Single photon emission from silicon-vacancy colour centres in chemical vapour deposition nano-diamonds on iridium

Elke Neu, David Steinmetz, Janine Riedrich-Möller, Stefan Gsell, Martin Fischer, Matthias Schreck, Christoph Becher

Angaben zur Veröffentlichung / Publication details:

Neu, Elke, David Steinmetz, Janine Riedrich-Möller, Stefan Gsell, Martin Fischer, Matthias Schreck, and Christoph Becher. 2011. "Single photon emission from silicon-vacancy colour centres in chemical vapour deposition nano-diamonds on iridium." *New Journal of Physics* 13: 025012. https://doi.org/10.1088/1367-2630/13/2/025012.

Single photon emission from silicon-vacancy colour centres in chemical vapour deposition nano-diamonds on iridium

New Journal of Physics
The open-access journal for physics

Single photon emission from silicon-vacancy colour centres in chemical vapour deposition nano-diamonds on iridium

Elke Neu[1], David Steinmetz[1], Janine Riedrich-Möller[1], Stefan Gsell[2], Martin Fischer[2], Matthias Schreck[2] and Christoph Becher[1,3]

[1] Universität des Saarlandes, Fachrichtung 7.2 (Experimentalphysik), Campus E2.6, 66123 Saarbrücken, Germany
[2] Universität Augsburg, Lehrstuhl für Experimentalphysik IV, Universitätsstrasse 1 (Gebäude Nord), 86135 Augsburg, Germany
E-mail: christoph.becher@physik.uni-saarland.de

New Journal of Physics **13** (2011) 025012 (21pp)
Received 27 August 2010
Published 21 February 2011
Online at http://www.njp.org/
doi:10.1088/1367-2630/13/2/025012

Abstract. We introduce a process for the fabrication of high-quality, spatially isolated nano-diamonds on iridium via microwave-plasma-assisted chemical vapour deposition (CVD) growth. We perform spectroscopy of single silicon-vacancy (SiV) centres produced during the growth of the nano-diamonds. The colour centres exhibit extraordinary narrow zero-phonon-lines down to 0.7 nm at room temperature. Single photon count rates up to 4.8 Mcps at saturation make these SiV centres the brightest diamond-based single photon sources to date. We measure for the first time the fine structure of a single SiV centre, thus confirming the atomic composition of the investigated colour centres.

[3] Author to whom any correspondence should be addressed.

Contents

1. Introduction

Single photon sources are of great interest for various applications in quantum information, in particular quantum cryptography (e.g. [1]). In recent years, colour centres in diamond have been proven to have the potential to fulfil the requirements for practical single photon sources, such as room temperature operation, photostability and high brightness. Nitrogen-vacancy (NV) centres [2]–[4], nickel-based NE8 centres [5]–[8], nickel–silicon complexes [9, 10], chromium-related colour centres [11, 12] as well as silicon-vacancy (SiV) centres [13] have been employed as single photon sources. The majority of the experiments have been performed on NV centres as they are easily available in single crystal diamonds [2] and in nanodiamonds [3], either produced during the growth process or by ion implantation. In addition, due to the extraordinarily long spin coherence times, key experiments towards quantum information processing have been realized with NV centres, e.g. two-qubit quantum gates [14] or quantum registers based on NV spins [15]. However, NV centres possess the detrimental property of a room temperature emission width of about 100 nm due to strong phonon coupling.

SiV centres were suggested as an alternative to NV centres due to their narrow zero-phonon-line (ZPL) width of 5 nm at room temperature, their low phonon coupling [13], as well as their feasible creation by ion implantation or during chemical vapour deposition (CVD) growth [18]. A further advantage is their emission in the near infrared at 738 nm in a spectral region where the background fluorescence of the surrounding diamond material is weak. First single emitter experiments on SiV centres created by ion implantation in natural diamonds [13], however, revealed unfavourable low single photon emission rates of the order of only 1000 counts s^{-1}, despite a short lifetime of 1.2 ns. Radiative quantum yields of only 0.05 were found for SiV centres in CVD films [19] and were explained by temperature-dependent non-radiative transitions, indicated by a strong increase in luminescence intensity for temperatures below 100 K [20]. Furthermore, the luminescence of SiV centres is quenched by the presence of graphite [16], thus defining the need for high-purity diamonds.

The structure of the SiV centre has been intensively investigated: it most probably consists of a silicon atom and a lattice vacancy arranged in a so-called 'split-vacancy configuration', where a substitutional silicon atom relaxes its position towards a neighbouring vacancy [21], as illustrated in figure 1. Photoluminescence excitation measurements suggest a position of the ground state of the centre 2.05 eV below the conduction band edge [16]. Spectroscopy of a

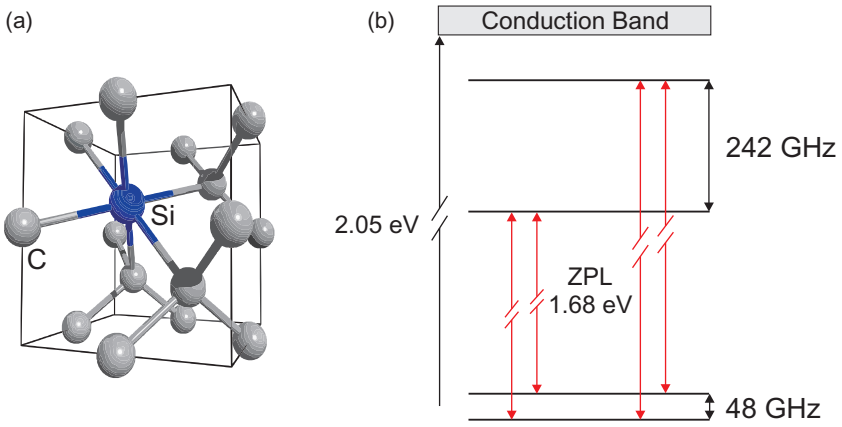

Figure 1. (a) Proposed structure of the SiV centre with a silicon atom in a split-vacancy site. (b) Level scheme of the SiV centre according to [16, 17]. The optical transitions are not drawn to scale.

high-quality single crystalline diamond at cryogenic temperatures reveals a fine structure of the ensemble ZPL consisting of four lines [17, 22]. A level scheme including a split excited state with components separated by 242 GHz and a split ground state with components separated by 48 GHz with four allowed optical transitions (see figure 1) was proposed to account for the observed fine structure [17]. This fine structure has never been observed for single SiV centres so far.

In this study, we present an advanced material system for single emitter spectroscopy of SiV centres: we employ a microwave-plasma-assisted CVD growth on nano-diamond-seeded iridium substrates to yield high-quality nano-diamonds. Single SiV centres are produced *in situ* during the CVD growth due to the presence of silicon impurities. Nano-diamonds exhibit superior properties as hosts for single photon sources as the fluorescence can be efficiently collected due to the lack of total internal reflection at the diamond–air interface [4]. We note that efficient collection of photons can also be achieved using nano-structures in single crystal diamond, e.g. diamond nano-wires [23]. A further advantage of nano-diamonds is a low fluorescence background due to the small diamond volume in the excitation laser focus. The iridium substrate provides optimized properties for our application: first of all, the metal substrate exhibits an extremely low fluorescence background. Secondly, spectroscopy on diamond films grown on iridium substrates did not reveal any substrate-specific luminescence in our experiments; thus, we conclude that growth on iridium does not lead to substrate-related colour centres. As a consequence, mostly luminescence-free nano-diamonds are produced. Furthermore, incorporation of the heavy element iridium into the dense crystal lattice of diamond is expected to be disfavoured as compared to many lighter elements (such as B, N and Si) due to its high atomic radius, enabling the growth of high-purity nano-diamonds. Finally, the iridium layer has the potential to alter significantly the radiative properties of the colour centres: in the presence of a metal layer, the electromagnetic field of an emitting dipole interacts both with the metal via near-field coupling and with the dipole itself via radiation back-action [24, 25]. The resulting effects include reduction of excited-state lifetimes, enhanced excitation probabilities, as well as enhanced collection efficiency due to radiation pattern modification, and depend critically on the distance of the emitter to the metal layer. Such effects have been investigated in detail for various single emitters, e.g. single molecules [24] or single CdSe quantum dots [26].

2. Experimental

2.1. Sample preparation

Nano-diamonds were grown on substrates consisting of a 150 nm thick iridium layer deposited onto a 40 nm thick buffer layer of yttria-stabilized zirconia on silicon [27]. For the growth process, $10 \times 10\,\mathrm{mm}^2$ substrates were used. Prior to the seeding procedure, the substrates were cleaned in permonosulfuric acid and rinsed in purified distilled water to remove possible contamination. The seeding procedure employed an aqueous solution of fully de-agglomerated synthetic nano-diamonds (Microdiamant Liquid Diamond MSY) with sizes up to 30 nm, which was spin coated onto the substrates. The size distribution of the seed nano-diamonds as measured by the manufacturer is displayed in figure 3(a): the maximum of the distribution is approximately 17 nm, with a full-width at half-maximum of about 12 nm. By diluting the solution, we are able to conveniently tune the seed density attained by the spin coating. For the investigated samples, the solution was diluted to contain approximately 0.6 mg of diamond per litre of solution. The seed density estimated from scanning electron microscope (SEM) images is roughly 2.5 seeds per $\mu\mathrm{m}^2$.

The seeded substrates were subjected to a microwave-plasma-assisted CVD process for 25 min. A hydrogen–methane plasma containing 1% methane at a gas pressure of 30 mbar and a microwave power of 2000 W was employed. SiV centres are created during CVD growth due to the presence of silicon impurities originating from the plasma exposure of the silicon substrates at the cut edges of the samples. Regarding the origin of silicon impurities, it cannot be excluded that the plasma in contact with the quartz wall of the reactor etches and transfers some additional silicon to the gas phase. However, etching of reactor walls and incorporation of silicon can be controlled to a large extent by the size of the plasma ball or the composition of the gas phase [28]. On the other hand, if silicon is used as a substrate, we observe the formation of ensembles of SiV centres in isolated nano-diamonds, similar to the findings of [29], but never single SiV centres. In this case, the efficient creation of SiV centres is attributed to the plasma etching of the exposed substrate [29, 30]. Thus, we assume that the silicon substrate is a major source of silicon impurities for growth on the iridium layer system as well.

Morphological characterization of the nano-diamonds was performed using a high-resolution SEM (Jeol JSM-7000 F). Figure 2(a) displays an overview of an $8 \times 6\,\mu\mathrm{m}^2$ area of the sample, confirming the growth of isolated nano-diamonds with a density of 1.7–2.2 CVD nano-crystals per $\mu\mathrm{m}^2$, slightly lower than the estimated seed density. Detailed images (figure 2(b)) reveal well-faceted nano-diamonds. The nano-diamonds show various crystal orientations, reproducing the different orientations of the seed crystals [29]. In principle, however, the iridium layers provide an additional option due to their unique properties as heteroepitaxy substrate for diamond(001) [27] and diamond(111) films [31]: synthesis of epitaxial diamond nano-crystals on iridium would yield SiV centres residing in a well-aligned diamond matrix, giving rise to a reproducible and well-defined orientation of the colour centre dipole.

By analysing the SEM images, we obtain the size distribution of the nano-diamonds displayed in figure 3(b). We identify a mean size of the crystals of 130 nm with a standard deviation of 40 nm. The distribution is slightly asymmetric, decaying more slowly towards small crystal sizes, thus qualitatively resembling the size distribution of the seed diamonds.

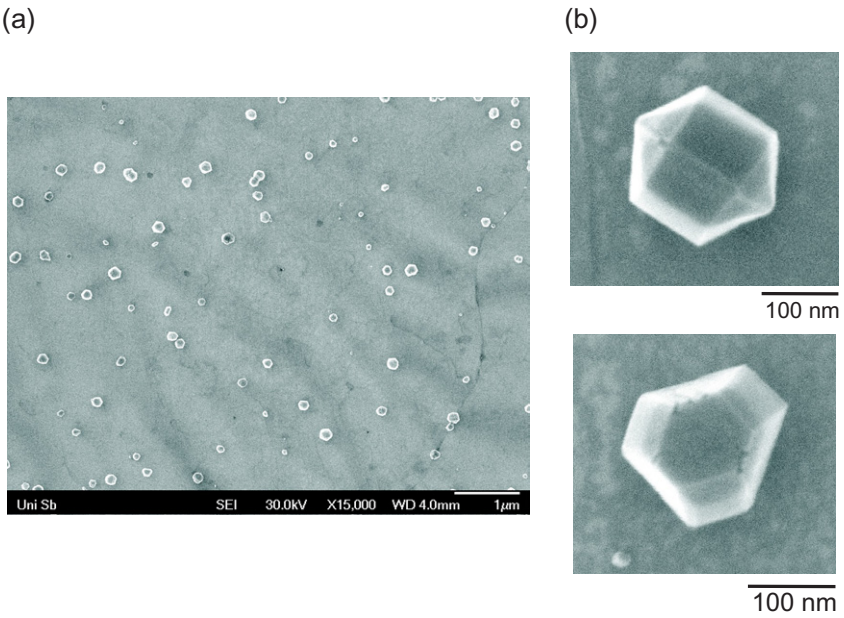

Figure 2. SEM images of CVD nano-diamonds. (a) Overview image area $8 \times 6\,\mu\text{m}^2$; (b) detailed images of typical well-faceted nano-diamonds.

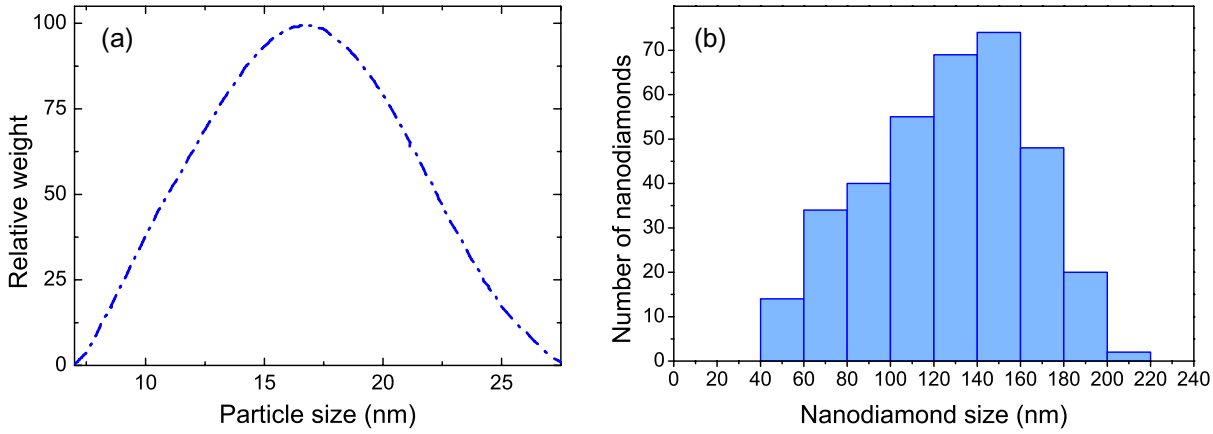

Figure 3. (a) Size distribution of the nano-diamonds used for the seeding process, as measured by the manufacturer. (b) Histogram of nano-diamond sizes after 25 min of growth. An overall number of 355 nano-diamonds were evaluated. The overall sample area under investigation was $240\,\mu\text{m}^2$. The sizes are averaged values, neglecting the different orientations of the diamonds.

The measurements described in the following were performed without any post-growth treatment of the nano-diamonds. With the given density of nano-crystals, roughly one bright SiV centre is observed in $50 \times 50\,\mu\text{m}^2$, thus enabling feasible single emitter characterization.

2.2. Experimental setup

To analyse the nano-diamond fluorescence, we use a confocal microscope setup. As the excitation source, a 671 nm frequency-doubled DPSS laser focused through a microscope

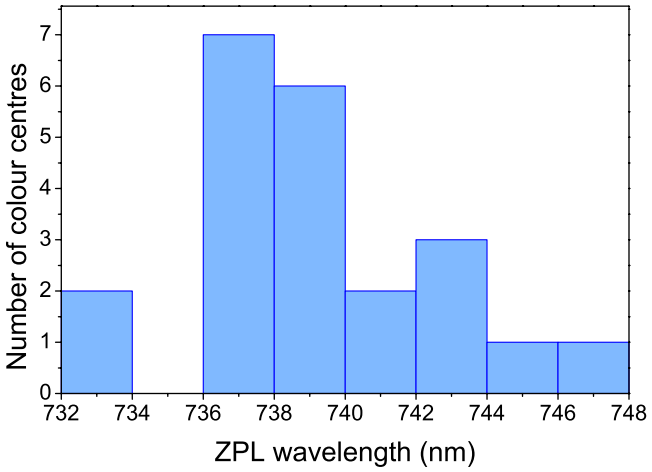

Figure 4. Histogram of the observed ZPL wavelengths of 22 colour centres. For the histogram, also nano-diamonds with multiple colour centres were taken into account.

objective with NA = 0.8 is employed. By using a dichroic beamsplitter and dielectric filters, the fluorescence in the spectral range of 730–750 nm is separated from reflected laser light and coupled into a multimode fibre simultaneously serving as a pinhole for the confocal setup. The fluorescence is directed to a Hanbury–Brown–Twiss setup (HBT) employing two avalanche photodiodes (APDs) (Perkin Elmer SPCM-AQRH-14) to measure the intensity autocorrelation g^2 of the emitted photons.

For spectral characterization, the fluorescence is analysed by a grating spectrometer (Horiba Jobin Yvon, iHR 550). For room temperature (cryogenic temperature) spectroscopy, we employ a grating with 600 (1800) grooves mm^{-1}, yielding a resolution of approximately 0.18 (0.06) nm, respectively. Taking into account the quantum efficiency of the APDs (typically 70%), the solid angle fraction corresponding to the NA of the objective and the transmission of the optical components, we estimate an overall detection efficiency of $\eta = 5.5\%$. To facilitate single emitter characterization at cryogenic temperatures, a flow cryostat (Janis Research, ST-500LN) operated with liquid helium is used.

3. Results

3.1. Single emitter spectroscopy at room temperature

3.1.1. Emission spectra. Confocal scans of the samples reveal nano-diamonds with bright luminescence in the spectral range 730–750 nm. A histogram of the observed lines is shown in figure 4. For the histogram, crystals containing single and multiple colour centres were taken into account. The measured line positions spread from 732 to 748 nm, although the majority of the observed colour centres show a ZPL between 736 and 740 nm. From investigations of poly-crystalline diamond films, ensembles of SiV centres are known to exhibit a room temperature line width of 6 nm with a temperature-independent inhomogeneous line width of up to 4.4 nm [32], depending on film quality. Thus, the inhomogeneous broadening of the SiV centre emission explains most of the observed spread of the line positions.

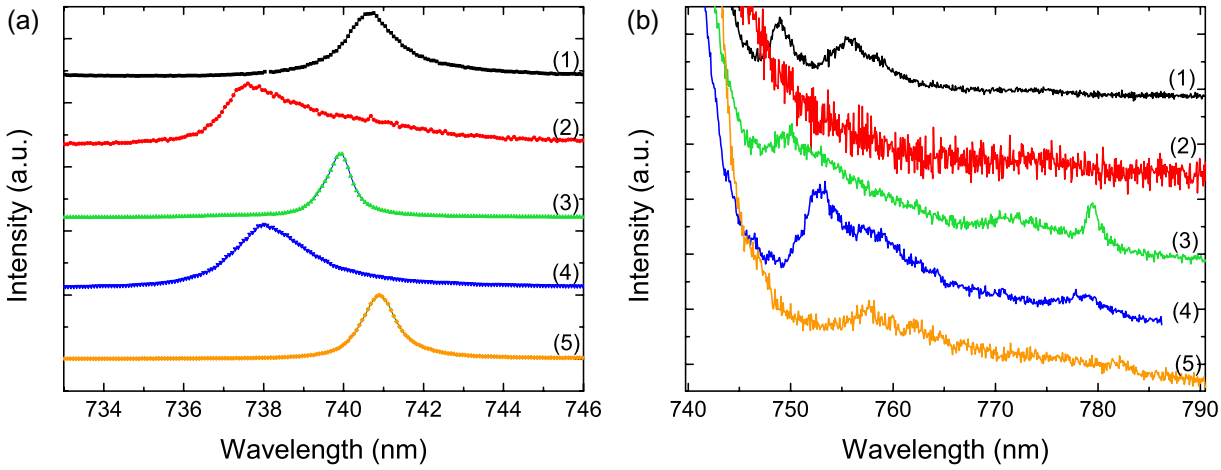

Figure 5. Room temperature spectra of the five colour centres under investigation. (a) ZPLs of the colour centres. The spectra have been normalized and displaced for clarity. (b) Sideband structure of the emitters. Spectra have been scaled and displaced to give a clear impression of the sideband structure.

Table 1. Overview of the luminescence parameters for the five different colour centres presented in this paper labelled emitters (1)–(5). λ_{Peak} is the peak wavelength of the ZPL and $\Delta\lambda$ its width. P_{sat} gives the saturation power from fitting equation (1) and I_{sat} the respective saturation intensity. I_{∞} denotes the single photon count rate at saturation. Finally, the Debye–Waller factor (DW) and the Huang–Rhys factor (S) are listed.

Emitter	λ_{Peak} (nm)	$\Delta\lambda$ (nm)	P_{sat} (μW)	I_{sat} (kW cm^{-2})	I_{∞} (kcps)	DW	S
(1)	740.7	1.6	14.3	1.2	263	0.76	0.28
(2)	737.6	1.2	43.0	3.7	512	0.84	0.18
	738.7	2.0					
	740.8	4.9					
(3)	739.9	0.7	40.9	3.5	395	0.79	0.24
(4)	738.2	2.2	306.7	26.1	4828	0.75	0.29
(5)	740.9	1.0	73.4	6.2	2395	0.88	0.13

In the following, we present a detailed characterization of five different single colour centres in individual nano-diamonds. Figure 5(a) displays spectra of the ZPLs of these centres. The peak positions range from 737.6 to 740.9 nm. Emitter (2) exhibits an asymmetric line shape, which is fitted best by introducing three lines at the positions listed in table 1. Remarkably, all colour centres display a room temperature ZPL line width of less than 2.2 nm. Emitter (3) shows a line width of only 0.7 nm, which is to our knowledge the narrowest room temperature line width measured for a diamond colour centre up to now. Thus, the line widths obtained are comparable to NE8 centres (1.2 nm [6] and 1.5 nm [8]) delivering the narrowest line widths so far and superior to the line widths observed for single SiV centres in previous studies (5–7 nm [13, 33]). The observed narrowing of the ZPLs compared to previous studies might be

Table 2. Overview of sideband features observed for the different emitters. For comparison, sidebands observed in previous works are listed. All energies are given in meV.

Emitter	S_{obs}	S_{Lit}	S_{obs}	S_{Lit}	S_{obs}	S_{Lit}	S_{obs}	S_{Lit}	S_{obs}	S_{Lit}
(1)	18.3	–	33.7	38.0 [36]	–	–	–	–	–	–
(2)	–	–	–	–	–	–	–	–	79.2	83.0 [36]
(3)	22.6	–	–	–	–	–	69.6	65.8 [32]	84.1	85.0 [22]
(4)	–	–	32.8	38.0 [36]	43.9	42.3 [32]	–	–	88.0	85.0 [22]
(5)	–	–	36.9	38.0 [36]	46.8	42.3 [32]	–	–	88.4	85.0 [22]

related to the broadening mechanisms involved: as described e.g. in [34], the width of the ZPL at room temperature is determined by homogeneous broadening due to electron–phonon scattering induced by a quadratic electron–phonon interaction. This broadening relates to the phonon density of states, which critically depends on local lattice distortions. Such local variations are visible e.g. in varying phonon sideband spectra, as discussed below. Thus, we assume that the high crystal quality of our nano-diamonds and a low impurity content might be responsible for the narrow ZPLs observed.

Another important issue for the use of colour centres as single photon sources is that the strength of the electron–phonon coupling determines both the fraction of the emission into the ZPL and the overall emission bandwidth including the phonon sidebands. The phonon coupling is measured by either the (Debye–Waller) DW factor or the Huang–Rhys factor (S). The DW factor is defined as the integrated luminescence intensity of the ZPL I_{zpl} divided by the integrated luminescence intensity of the colour centre I_{tot} [6]. The Huang–Rhys factor S is defined by $\frac{I_{zpl}}{I_{tot}} = \exp(-S)$ [35]. As listed in table 1, emitters (1), (3) and (4) show DW factors of 0.75–0.79 corresponding to Huang–Rhys factors of 0.29–0.24, thus corresponding very well to $S = 0.24$ determined for ensembles of SiV centres [18]. Emitters (2) and (5) exhibit further reduced phonon coupling, resulting in DW factors of 0.84 and 0.88, respectively. The structure of the vibronic sidebands of the emitters is depicted in figure 5(b). Table 2 summarizes the energies of the observed features with respect to the ZPLs. The sidebands measured here resemble sidebands previously observed for SiV ensembles, especially at about 38–42, 65 and 83–85 meV, as indicated in table 2.

Despite these similarities, the vibronic sideband spectra of individual crystals differ significantly. A related effect has been reported by Gorokhovsky *et al* [32] for SiV ensembles in poly-crystalline CVD films: only by resonant excitation selecting a narrow sub-ensemble, a clear sideband structure was observed, while it was washed out for off-resonant excitation due to inhomogeneous effects in the different crystals. Similar considerations are relevant for isolated nano-diamonds taking into account size effects and stress in individual nano-diamonds.

3.1.2. Single photon count rates. As an important figure of merit for a single photon source, we investigate the photon count rate obtained at saturation. Figure 6 displays the saturation curves for the five emitters under investigation. The count rate I in dependence of the excitation power P has been fitted with the function

$$\mathrm{I} = I_\infty \frac{P}{P + P_{sat}}. \tag{1}$$

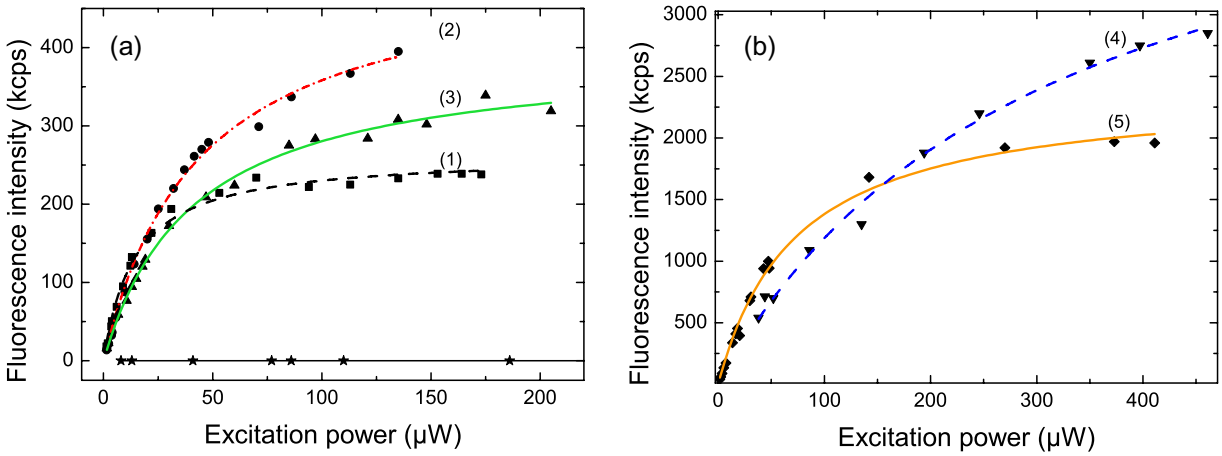

Figure 6. Single photon count rates of the five colour centres under investigation, recorded as a function of excitation power. (a) Count rates of emitters (1)–(3); (b) count rate of emitters (4) and (5). The lines display the fitted functions according to equation (1). The parameters obtained from the fitted functions are summarized in table 1. In (a), the typical background level recorded on the substrate is displayed (filled stars).

Fitting parameters are the saturation power P_{sat} and the maximum obtainable count rate I_∞. The values determined from the fitted curves are summarized in table 1. By taking into account the transmission of the laser light through the microscope objective and the spot size of the focus ($1/e^2$ radius) of approximately 0.51 μm, we estimate the intensity impinging on the emitters. The results are also presented in table 1.

Emitter (2) exhibits a remarkably low saturation power of only 14.3 μW, indicating a very efficient excitation path. In previous studies [13], a saturation power of 6.9 mW for an excitation wavelength of 685 nm was determined. The very efficient excitation observed here with saturation powers below 310 μW for all emitters allows for a significant reduction of the background fluorescence. In figure 6(a), the typical background level on the substrate 2 μm away from a luminescent nano-diamond is displayed. Even for the highest excitation powers, a background of only 1.5 kcps is observed. Thus, the background fluorescence from the substrate is at least 175 times lower than typical fluorescence rates observed, demonstrating a major benefit of the iridium substrate. Note that this does not give reliable information about the signal-to-background ratio obtained for the emitters: the background due to fluorescence of the nano-crystal cannot be directly measured as it cannot be separated from the colour centre luminescence. Nevertheless, the properties of the measured g^2 functions confirm very high signal-to-background ratios as discussed in section 3.1.4.

The observed photon count rates show large variation: emitters (1)–(3) display maximum count rates between 263 and 512 kcps, whereas emitters (5) and (4) feature maximum count rates of 2.4 and 4.8 Mcps. The latter rate, to our knowledge, is the highest photon count rate observed for a single colour centre in diamond until to now, surpassing recently investigated single photon sources based on chromium colour centres delivering a maximum of 3.2 Mcps [11]. Furthermore, the count rate observed here is more than three orders of magnitude higher than the count rates obtained in previous studies on SiV centres in single crystal

diamond (approximately 1000 cps, [13]). The enhancement compared to the count rates for SiV centres in bulk diamond is not exclusively explained by the enhanced fluorescence extraction efficiency from the nano-crystals compared to bulk diamond, which has been measured to enhance the fluorescence rate by a factor of 11 [33]. Moreover, the good crystalline quality of the nano-diamonds as observed in SEM investigations might lead to enhanced fluorescence properties if non-radiative processes are suppressed. Additionally, the presence of the iridium layer influences the fluorescence properties by narrowing the emission cone of the colour centres, thus enhancing the collection efficiency [24, 26]. The iridium layer might also lead to a weak enhancement of the radiative decay rates of the colour centres as well as a significant enhancement of the non-radiative decay rates due to near-field coupling and absorption (see section 3.1.4). As these effects depend critically on the distance of the emitting dipole from the metal layer, they vary with the unknown position of different emitting colour centres inside our nano-diamonds of about 130 nm size, thus contributing to the spread in count rates. In addition, the undefined dipole orientation of the colour centres gives rise to changes in collection efficiency: for the microscope objective employed (NA = 0.8), the collection efficiency varies by a factor of 2.4 for dipoles oriented perpendicular and parallel to the optical axis of the microscope objective [37]. Finally, as discussed in section 3.1.4, the observed colour centres also exhibit different population dynamics, including the participation of shelving states leading to different brightnesses.

The investigated emitters did not show blinking; nevertheless, emitter (4) was permanently photobleached after approximately one and half hours of observation when applying high excitation power to carry out the saturation measurement. If a change in the charge state was responsible for the bleaching, enhanced stability might be gained by controlling the surface termination of the nano-diamonds, as shown for NV centres [38]. Another route might be by enlarging the nano-diamond size to reduce surface effects. These approaches are currently under investigation.

3.1.3. Polarization measurements. The polarization properties of the colour centres play a crucial role in their use as single photon sources: if the colour centre preferentially absorbs linearly polarized light, one can optimize the excitation by choosing the fitting linear polarization, thus gaining signal-to-background ratio. Linearly polarized emission is advantageous for applications of single photon sources, e.g. in quantum cryptography (BB84 protocol), which require photons of a defined polarization. To measure the polarization properties of the colour centres in absorption, a half-wave plate is used to rotate the polarization angle of the excitation laser light. To determine the polarization properties of the emitted photons, we use a linear polarization analyser in the detection path. Figure 7 displays the curves measured for selected emitters. The intensity I as a function of the polarizer angle is fitted using a sine-square function. To describe the contrast obtained we calculate the visibility V,

$$V = \frac{I_{\max} - I_{\min}}{I_{\max} + I_{\min}}. \tag{2}$$

Table 3 summarizes the visibilities obtained from the measurements. If the colour centre can be described as a single dipole in absorption, we expect a visibility of close to 100% [39] with a change from maximum to minimum intensity corresponding to a change in polarization angle of 90°. This behaviour is basically observed for emitters (1), (2) and (4), although the contrast does not reach 100%. The deviation is mainly due to polarization changes induced

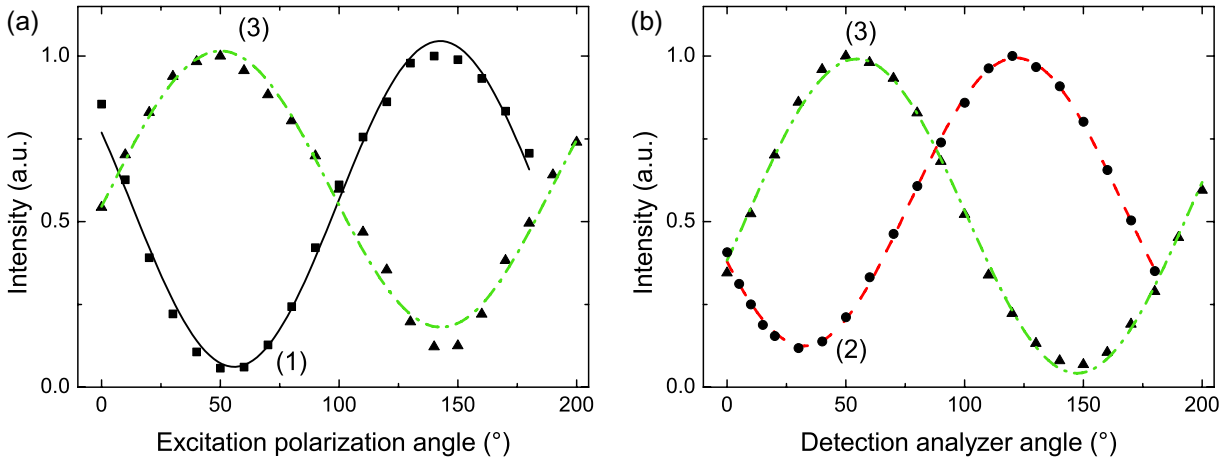

Figure 7. Polarization-dependent count rates of selected emitters (a) as a function of excitation polarization, and (b) for a fixed excitation polarization but dependent on the analyser angle. Note that the position of the minima and maxima shifts for different emitters due to the varying orientation of the colour centres in the nano-crystals.

Table 3. The visibility of the polarization-dependent intensity. V_{exc} denotes the visibility obtained by rotating the excitation polarization. V_{pl} denotes the visibility obtained by rotating a linear polarization analyser in the detection path while keeping the excitation polarization fixed. For emitter (4), the polarization of the luminescence has not been measured.

Emitter	V_{exc} (%)	V_{pl} (%)
1	88.9	87.6
2	83.0	77.7
3	78.0	91.0
4	84.9	–
5	70.0	84.3

by the dichroic beam splitter: for s- and p-polarization, the dichroic mirror does not change the polarization of the laser light, whereas for light polarized at 45°, we observe a loss of linear polarization degree of 10%. Thus, the depolarization due to the beam splitter might give an explanation for the reduced visibility for emitters (1), (2) and (4), yielding evidence for single dipole behaviour in excitation. However, as the visibility amounts to only 70 and 78% for emitters (3) and (5), the contribution of a second dipole to the excitation as e.g. observed for the NV centre [40] cannot be excluded.

For the emitted fluorescence, similar experimental considerations hold: when passing the dichroic mirror, polarization angle-dependent rotation and loss of linear polarization occur. These effects have been qualitatively observed for reflected laser light. Further investigations have to show whether the loss in linear polarization degree is due to an elliptical polarization, as stated in [7]. Thus, due to depolarizing effects, we do not expect to observe 100% visibility even for fully linear polarized emission. Furthermore, as a consequence of the angle-dependent

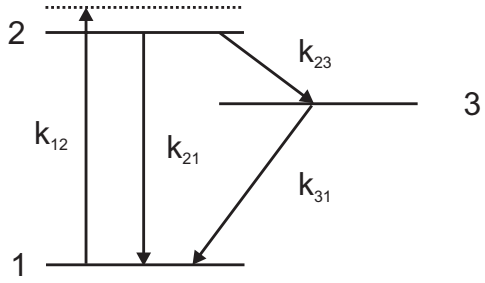

Figure 8. Schematic representation of the three-level model employed to explain the population dynamics of the colour centres.

polarization rotation effects, the polarization angle measured behind the dichroic mirror differs from the polarization angle of the emitted light. In addition to the depolarizing effects in the detection path, we have to take into account the loss of polarization contrast due to imaging with a high NA objective [41]: the polarization visibility of a single dipole depends critically on its orientation: for a dipole with its axis perpendicular to the optical axis of the microscope, 100% visibility is theoretically obtained. On the other hand, for a dipole with its axis parallel to the optical axis of the microscope objective, no net contrast is obtained as the polarization is not constant over the collimated fluorescence beam ('polarization anisotropy'). As the orientation of the nano-diamonds on the sample is random, the orientation of individual SiV centre dipoles is random as well. Thus, we are in principle not able to determine whether a polarization contrast deviating from 100% is due to the orientation-dependent loss of contrast or due to a possible contribution of a second dipole moment.

In our experiments on polarization contrast of SiV fluorescence, three emitters (1), (3) and (5) show high visibilities of 87.6, 91 and 84.3%, respectively. On the basis of the experimental considerations described above, we can assume that these emitters show close to 100% visibility of the emitted light, thus evidencing single dipoles oriented approximately perpendicular to the optical axis of the setup. The measured visibility of emitter (2) amounts to only 77.7%. Here, we cannot identify whether the dipole is oriented at an angle between 0° and 90° to the optical axis or a second dipole contributes to the transition. To our knowledge, the nature of the electronic states of the SiV centre is still subject to debate [17, 21], and no investigations into dipoles contributing to transitions of the SiV centre have been reported in the literature. Thus, this topic needs further investigation.

3.1.4. Photon correlation measurements and theoretical modelling. To prove the single emitter behaviour and to analyse the population dynamics of the investigated colour centres, measurements of the g^2 function for different excitation powers have been carried out. The results are displayed in figures 9–11. As a signature of single emitters, all curves show a pronounced antibunching dip at zero delay. Additionally, the measured g^2 functions exceed values of one for longer time scales, giving rise to a bunching behaviour. The bunching signature is intensity dependent, becoming more pronounced for higher excitation powers: for emitter (1), g^2 values exceeding 10 are measured. The measurements also reveal differences in this bunching behaviour for the emitters: whereas for emitter (1) bunching becomes only visible for excitation well above saturation, all other emitters exhibit photon bunching already for lower power. The time constants governing the bunching behaviour show a large variation among

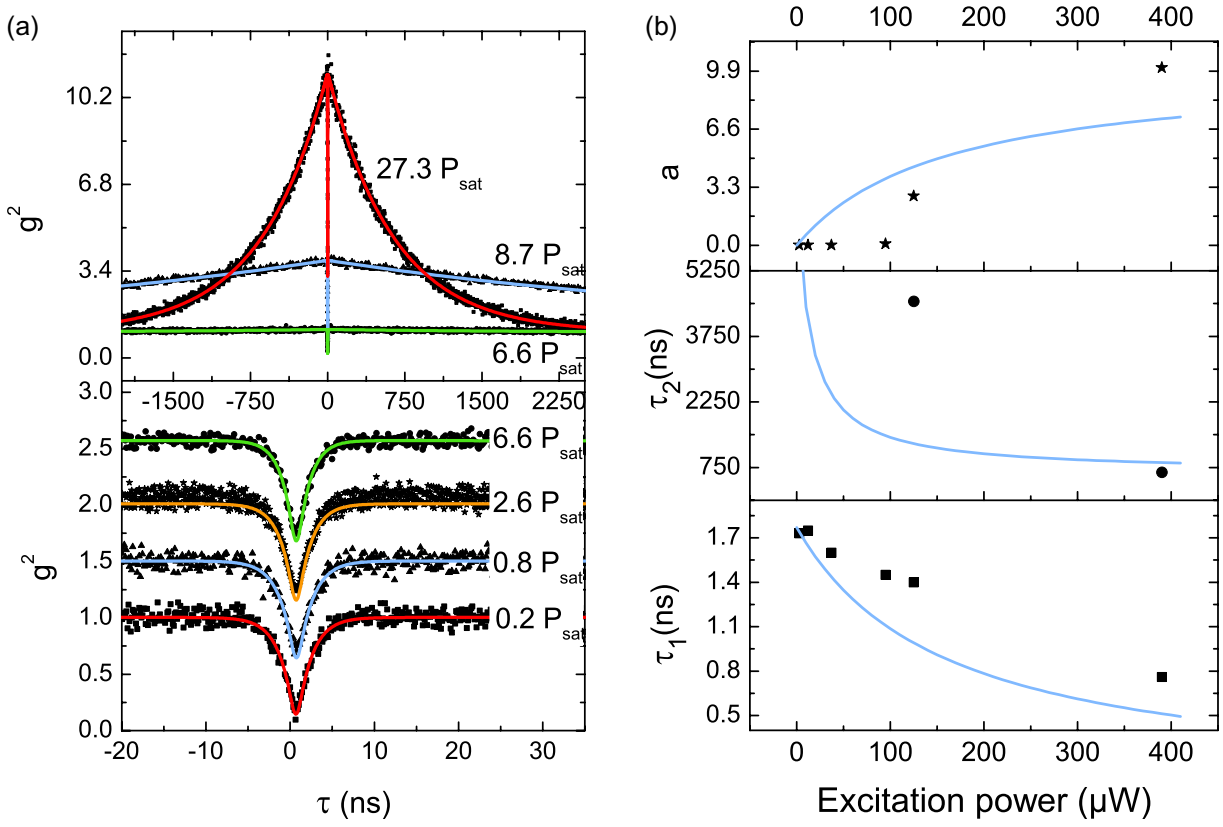

Figure 9. Population dynamics of emitter (1). (a) The g^2 functions for different excitation powers, given in units of the saturation power $P_{\mathrm{sat}} = 14.3\,\mu$W. For lower excitation power, the region of short delays is plotted (lower graph), while for higher powers, a larger region of delays is plotted, to permit observation of the bunching behaviour. Note that for low power, consecutive g^2 functions have been displaced by 0.5 for clarity. Fits confirm that the residual $g^2(0)$ values are due to the timing jitter only, unambiguously proving single emitter behaviour. (b) Constants τ_1, τ_2 and a obtained from the g^2 functions. The constants τ_2 for $P < 125\,\mu$W are not given as they could not be reliably determined due to the very low value of a.

the emitters: the g^2 function of emitter (4) decays to a value of one for time delays of less than 50 ns even at low power, whereas for emitters (1)–(3), time constants of more than 1 μs are observed for low power, decreasing to below 100 ns for high excitation power.

To explain this behaviour, a three-level system including a 'shelving state' has to be considered. As the nature of the participating states is unknown, we use in a first approach the simplified model depicted in figure 8: we assume that the excitation rate of level 2 depends linearly on the excitation power P: $k_{12} = \sigma P$. Levels 1 and 2 are coupled via a fast radiative transition with the rate coefficient k_{21}, whereas level 3 acts as a 'shelving state' populated via the rate coefficient k_{23} with the possibility of relaxation into the ground state via k_{31}. As long as the emitter resides in state 3, no photons on the radiative transition $2 \rightarrow 1$ are detected. This simple model has been successfully employed to describe the dynamics of molecules involving

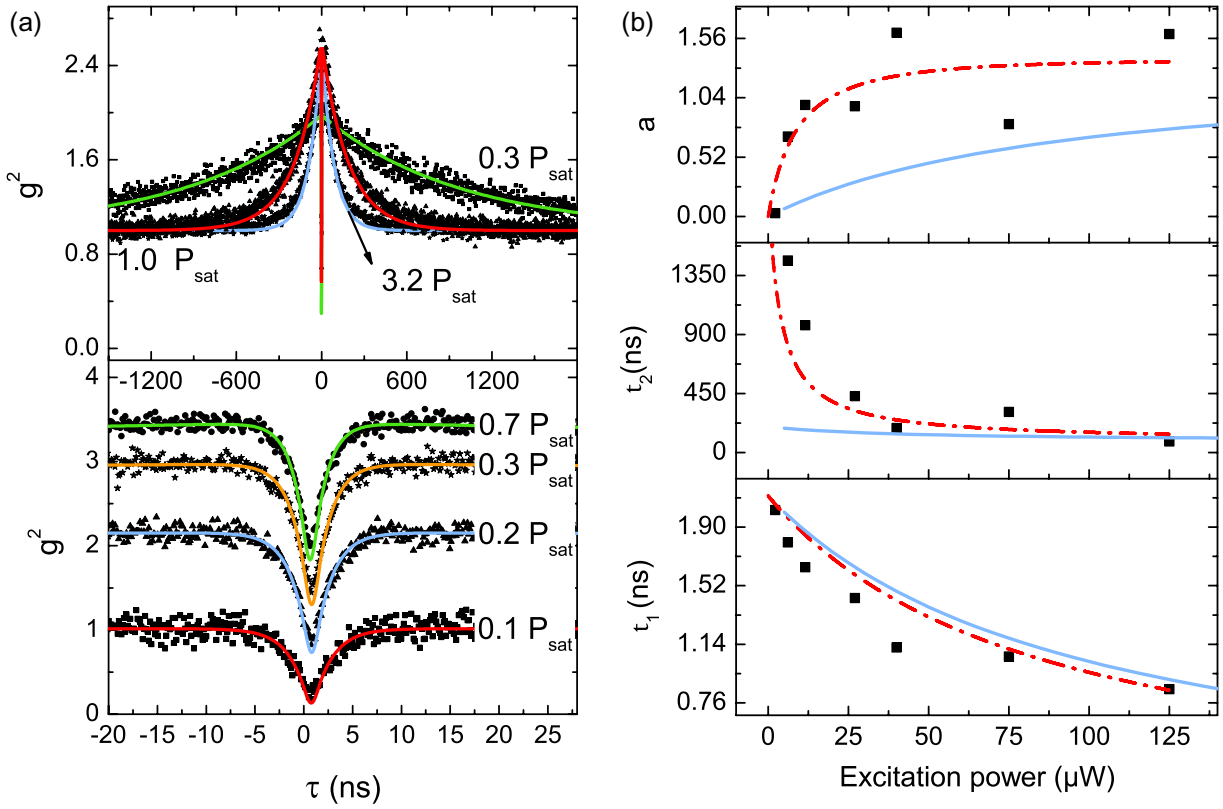

Figure 10. Population dynamics of emitter (3). (a) g^2 functions for different excitation powers, given in units of the saturation power $P_{\mathrm{sat}} = 40.9\,\mu$W. For lower excitation power, the region of short delays is plotted (lower graph), while for higher powers a larger region of delays is plotted, to permit observation of the bunching behaviour. Note that for low power, consecutive g^2 functions have been displaced by 0.5 for clarity. Fits confirm that the residual $g^2(0)$ values are due to the timing jitter only, unambiguously proving single emitter behaviour. (b) Constants τ_1, τ_2 and a obtained from the g^2 functions. Solid blue lines: intensity dependence obtained from the simple three-level model; dashed red lines: intensity dependence obtained from the extended model, including an intensity-dependent de-shelving.

shelving states [42]. Due to the very pronounced bunching behaviour at high powers, we exclude efficient power-dependent de-shelving processes, as described in [7, 11], and thus assume, in a first approach, constant shelving and de-shelving rates k_{23} and k_{31}, respectively. The g^2 function describes the dynamics and is defined by $\frac{n_2(\tau)}{n_2(\tau\to\infty)}$, resulting in

$$g^{(2)}(\tau) = 1 - (1+a)\,\mathrm{e}^{-|\tau|/\tau_1} + a\,\mathrm{e}^{-|\tau|/\tau_2}. \tag{3}$$

The parameters a, τ_1 and τ_2 are given by [33]

$$\tau_{1,2} = 2/(A \pm \sqrt{A^2 - 4B}), \tag{4}$$

$$A = k_{12} + k_{21} + k_{23} + k_{31}, \tag{5}$$

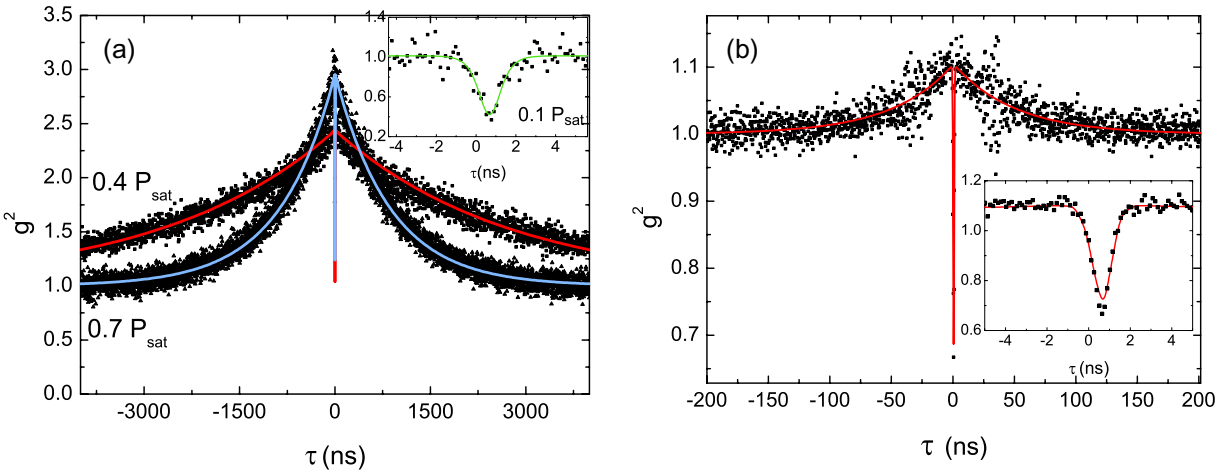

Figure 11. g^2 functions for emitters (2) and (4). (a) Power-dependent g^2 functions for emitter (2). The inset displays the antibunching dip at $0.1P_{\text{sat}}$ in detail. The fit confirms that the residual $g^2(0)$ is due to the timing jitter and the short $\tau_1 = 0.45$ ns constant only, confirming single emitter behaviour. (b) g^2 function of emitter (4) at $P = 0.15P_{\text{sat}}$. The inset shows the antibunching dip in detail; again, the residual g^2 is governed by the jitter only, confirming single emitter behaviour with $\tau_1 = 0.21$ ns.

$$B = k_{12}k_{23} + k_{12}k_{31} + k_{21}k_{31} + k_{23}k_{31}, \tag{6}$$

$$a = \frac{1 - \tau_2 k_{31}}{k_{31}(\tau_2 - \tau_1)}. \tag{7}$$

To describe the experimental results correctly, we have to account for the timing jitter of the APDs used. To this end, we convolute equation (3) with the measured Gaussian response function of our setup ($1/\sqrt{e}$ width 354 ps). Figures 9–11 display the measured curves, including the fits of equation (3) convoluted with the response function. The deviation from the expected value $g^2(0) = 0$ for a single emitter is fully explained by the timing jitter of the setup for low excitation power, thus unambiguously proving single emitter behaviour for the observed colour centres. Note that no correction for background luminescence was necessary to obtain these results, confirming negligible background contributions. We note that this also holds for higher excitation powers: for excitation powers of about P_{sat} (emitters (1)–(3)), the deviation of the fitted $g^2(0)$ from the measured value is still only about 0.1. The results of the photon correlation measurements are thus consistent with values of $g^2(0) \leqslant 0.1$.

The τ_1 parameters at low excitation powers, indicating the lifetime of the excited state under the assumption $k_{21} \gg k_{23} + k_{31}$, which is valid in our case, as shown later, show a large variation from 2 ns for emitter (3) down to 0.2 ns for emitter (4). The variation of the observed excited state lifetimes might be due to several reasons. Firstly, the SiV centre is assumed to possess a strong non-radiative decay channel [19]. This non-radiative decay channel varies with local strain in different nano-diamonds [20]. Secondly, the excited state lifetime is modified by the presence of the metal layer. To estimate this influence, we perform three-dimensional finite-difference time domain calculations (FDTD Solutions, Lumerical). To simplify the problem, we assume an emitting dipole in a semi-infinite diamond slab (refractive index $n = 2.4$) above a

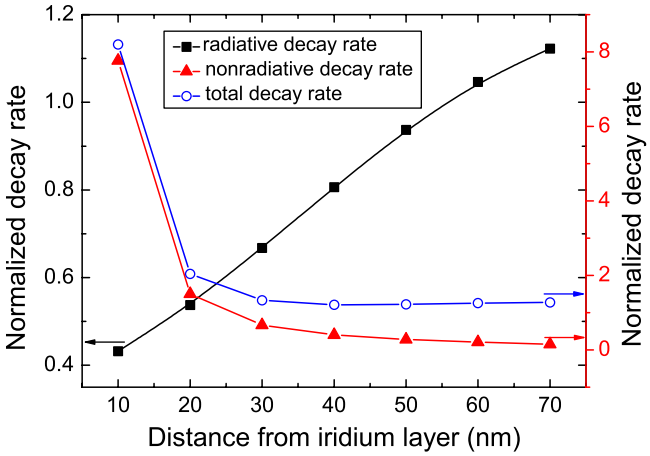

Figure 12. Decay rates of an emitting dipole in diamond parallel to an iridium layer for different distances from the layer. The decay rates have been normalized to the rates of the dipole embedded in diamond without the presence of the iridium layer.

semi-infinite iridium layer ($\epsilon = -18 + \mathrm{i} \cdot 25$ at 740 nm [43]). As the orientation of the emitting dipole is unknown, we simulate a dipole parallel to the iridium layer as a first estimate. The influence of the metal layer can be divided into two regimes: at distances $\gtrsim \frac{\lambda}{2}$ ($\approx$155 nm in diamond for the investigated colour centres), the lifetime usually shows an oscillatory behaviour due to far-field interaction of the dipole with its mirror image [24]–[26]. We disregard this regime as the diamond nano-crystals have a mean size of 130 nm and the emitter–metal distance thus is $\lesssim$130 nm. In figure 12, we present the results for the radiative and non-radiative as well as the total decay rates for a dipole parallel to the iridium layer at distances between 10 and 70 nm from the iridium surface. Note that the rates are normalized with respect to the decay rates of an equivalent dipole in bulk diamond. At these distances, there is a strong influence of the metal as the dipole near-field components efficiently couple to evanescent waves in the metal. The modification of the decay rates is especially pronounced for distances of less than 20 nm: due to the near-field coupling to the absorbing metal, the non-radiative decay rate is enhanced by a factor of eight, while the radiative decay is simultaneously lowered by more than a factor of two. For a distance of 60 nm, the decay rates roughly match the rates for the dipole without the presence of the iridium layer. Thus, the presence of the metal layer might account for a spread of approximately a factor of eight in the measured lifetimes due to the varying positions of the colour centres in the nano-diamonds. However, we note that the lifetime reduction does not lead to an enhanced radiative decay due to the quenching by the metal, in agreement with previous observations [24].

The rate coefficients k_{12}, k_{21}, k_{23} and k_{31} governing the population dynamics of the colour centres are derived from the limiting values of the fitted parameters a, τ_1 and τ_2,

$$k_{31} = \frac{1}{(1 + a^{\infty})\tau_2^{\infty}}, \tag{8}$$

$$k_{23} = k_{31} a^{\infty}, \tag{9}$$

$$k_{21} = \frac{1}{\tau_1^0} - k_{23} \quad \text{for} \quad k_{21} + k_{23} > k_{31}, \tag{10}$$

where the superscript $^{\infty}$ denotes the limit for high excitation power and ^{0} denotes the limit for vanishing excitation power. The values of a, τ_1 and τ_2 for emitters (1) and (3) are displayed in figures 9(b) and 10(b). The data indicate the limiting values of a, τ_1 and τ_2 despite the fact that some oscillatory behaviour is observed. This might be due to experimental reasons: above saturation, spatial drifts changing the intensity impinging on the emitter do no longer lead to measurable photon count rate changes, thus making the detection of drifts and ensuring constant excitation intensity very challenging. Nevertheless, a rough estimate of the rate coefficients is possible for emitters (1) and (3): we obtain $k_{21} = 564\,\text{MHz}$, $k_{23} = 1.4\,\text{MHz}$, $k_{31} = 0.14\,\text{MHz}$ for emitter (1) and $k_{21} = 469\,\text{MHz}$, $k_{23} = 6.7\,\text{MHz}$, $k_{31} = 5.0\,\text{MHz}$ for emitter (3). With these rate coefficients and the measured saturation power I_{sat}, we obtain the power dependence of a, τ_1 and τ_2 shown as solid lines in figures 9(b) and 10(b). The curves qualitatively resemble the observed behaviour with deviations especially for τ_2 and a at low powers.

In the following, we propose an extension of the simple three-level model in figure 8, allowing one to account for these deviations. For the discussion, we exemplarily use the data obtained from emitter (3). As an alternative to the limiting values used in equation (8), we now employ the limiting value of τ_2 for zero excitation,

$$k_{31} = \frac{1}{\tau_2^0}. \tag{11}$$

By using equation (11) instead of (8) together with equations (9) and (10), we obtain an 'alternative' set of rate parameters: $k_{21} = 465\,\text{MHz}$, $k_{23} = 11.3\,\text{MHz}$, $k_{31} = 0.49\,\text{MHz}$. Thus, the value of k_{31} seems to be inconsistent for high and low excitation powers, indicating an intensity-dependent de-shelving process. As mentioned before, we exclude a de-shelving process linearly dependent on excitation power [7, 11, 44], as this model would lead to

$$\tau_2^{\infty} = 0, \quad a^{\infty} = 0, \tag{12}$$

which is not consistent with our observations. We therefore tentatively modify the intensity dependence of the rate k_{31} to follow a saturation law, including an intensity-independent rate k_{31}^0,

$$k_{31} = \frac{d \cdot P}{P + c} + k_{31}^0. \tag{13}$$

The introduction of a saturating de-shelving process is further motivated by the possible explanation of this process as an excitation from the shelving state to higher-lying states, as e.g. found for molecules in [44]. This excitation process might intrinsically exhibit a saturation behaviour. For the new model, we calculate k_{23}, k_{21}, k_{31}^0 and d under the assumption $k_{21} + k_{23} > k_{31}^0$,

$$k_{31}^0 = \frac{1}{\tau_2^0}, \tag{14}$$

$$d = \frac{1/\tau_2^{\infty} - (1 + a^{\infty})/\tau_2^0}{a^{\infty} + 1}, \tag{15}$$

$$k_{23} = \frac{1}{\tau_2^{\infty}} - k_{31}^0 - d, \tag{16}$$

$$k_{21} = \frac{1}{\tau_1^0} - k_{23}. \tag{17}$$

For emitter (3), we obtain the following with equations (14)–(17) and a^∞, τ_1^0, τ_2^0 and τ_2^∞ derived from the measurements: $k_{31}^0 = 0.50\,\mathrm{MHz}$, $k_{23} = 6.72\,\mathrm{MHz}$, $k_{21} = 469.48\,\mathrm{MHz}$ and $d = 4.55\,\mathrm{MHz}$. Now the parameter c as well as the proportionality constant σ for the excitation rate $k_{12} = \sigma P$ can be determined by fitting the intensity-dependent data for a with equation (7) (σ is no longer accessible from the saturation measurement in this model). The results are shown in figure 10(b); we obtain $c = 98.1\,\mu\mathrm{W}$ and $\sigma = 5.72\,\mathrm{MHz}\,\mu\mathrm{W}^{-1}$. With these values of c and σ, the intensity dependence of τ_1 and τ_2 is also well described. We thus conclude that a complex power dependence of the de-shelving rate has to be accounted for to properly model the SiV centre dynamics. To prove the general validity of this model, it has to be tested on a larger number of emitters.

The rate coefficients determine the maximum obtainable photon count rate I_∞ for cw excitation and the maximum steady-state population of the excited state $n_2^\infty = n_2(\tau \to \infty, k_{12} \to \infty)$,

$$I_\infty = \eta_{\mathrm{coll}}\,\eta_{\mathrm{qe}}\,k_{21}\,n_2^\infty = \eta_{\mathrm{coll}}\,\eta_{\mathrm{qe}}\,\frac{k_{21}}{1 + (k_{23}/(k_{31}^0 + d))}. \tag{18}$$

For the simple three-level model, $k_{31}^0 + d$ has to be replaced by the intensity-independent rate k_{31}. As the orientation of the emitting dipole inside the nano-crystal is unknown, the actual collection efficiency η_{coll} includes an uncertainty of a factor of 2.4, as discussed in section 3.1.2. In addition, the rate coefficients have to be considered as a rough estimate; thus, determining the quantum efficiency η_{qe} from the measured photon rate is not reliable. Nevertheless, by using the rate coefficients, we illustrate the influence of the shelving state on the maximum photon count rate for cw excitation: for an off-resonantly pumped two-level system with decay rate k_{21}, we expect a maximum photon rate,

$$I_\infty = \eta_{\mathrm{coll}}\,\eta_{\mathrm{qe}}\,k_{21} n_2^\infty = \eta_{\mathrm{coll}}\,\eta_{\mathrm{qe}}\,k_{21}. \tag{19}$$

Thus, we deduce that for emitter (3) the presence of the shelving state changes the maximum photon rate only by about a factor of two as $n_2^\infty = 0.43$ compared to $n_2^\infty = 1$ for an off-resonantly pumped two-level system. In contrast, for emitter (1), the presence of the shelving state leads to $n_2^\infty = 0.09$, thus potentially lowering the maximum photon rate by a factor of more than 10. As the nature of the shelving state and the relaxation process is unknown, the reason for the differences in bunching behaviour remains unclear. We emphasize that the large spread in excited state lifetimes in combination with large differences in shelving state dynamics suffices to explain large variations in photon emission rates of SiV centres.

3.2. Single emitter spectroscopy at cryogenic temperatures

Spectroscopy of colour centres at cryogenic temperatures is an important issue for their application in quantum optics: underlying fine structures of ZPLs can only be observed at cryogenic temperatures reducing phonon broadening; additionally the determination of low-temperature line widths is crucial for applications involving coherent processes. We characterize emitter (5) at room temperature and at 30 K. Figure 13 displays the measured spectra. Note that g^2 measurements prove single emitter behaviour for both temperatures. Emitter (5) has a room temperature line width of 1 nm. Upon cooling to 30 K, a fine structure evolves consisting of four components at 740.42 nm, 740.11 nm, 739.19 nm and 738.91 nm. The line width of the individual components reduces to 0.17 nm. This four-line fine structure is characteristic of SiV centres and has so far been observed only for ensembles of SiV centres in single crystals of high

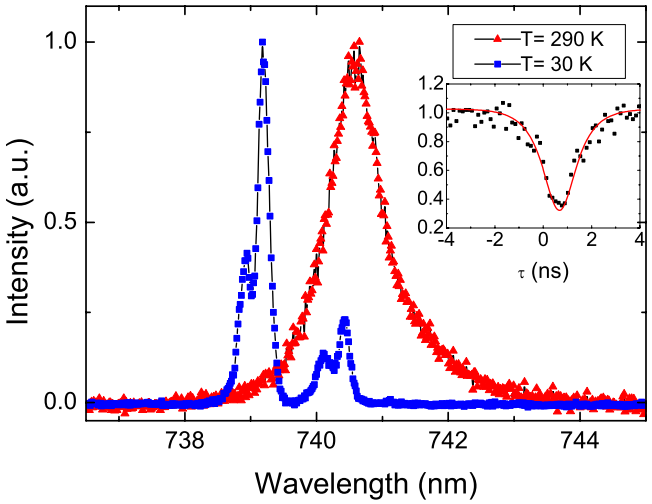

Figure 13. Temperature-dependent spectra of emitter (5). The spectra have been measured at 290 K (red triangles) and 30 K (blue squares). The inset displays the g^2 function of emitter (5) measured at 1.3 μW. The fit confirms that the residual $g^2(0)$ value is fully explained by the timing jitter of the setup, thus proving the existence of a single emitter.

quality [17, 22], thus providing significant evidence for the identification of the observed colour centres as SiV centres. The spacing of the outer components is 1.5 nm. For SiV centres in single crystals this spacing increases from 0.7 nm (no stress) to 2.4 nm by applying a stress of 0.5 GPa along the (001) direction [22]. Thus, the observed spacing can be explained by stress inside the nano-crystal. The spectrum shifts by 1.5 nm to shorter wavelengths when cooling to 30 K (highest fine structure peak compared to room temperature ZPL). This shift is also characteristic of SiV centres in poly-crystalline CVD diamonds: Ghorokovsky *et al* [32] as well as Feng and Schwartz [20] observed a blue shift of 1.4 and 1.2 nm, respectively, when cooling to 100 K and no further shift for lower temperatures. For the observed single SiV centre, the line shifting also stops around 110 K, thus resembling the observations for ensembles.

4. Conclusion

We have identified an advanced material system for single photon sources in diamond employing high-quality CVD nano-diamonds on iridium produced via spin coating seeding and microwave CVD growth. Due to impurities in the growth process, single SiV centres are formed. The iridium substrates together with the small-volume nano-diamonds provide a major advantage, namely single photon emission with negligible contributions of background fluorescence. Furthermore, the SiV colour centres observed here are much better than their reputation and exhibit very promising behaviour as single photon sources: line widths as low as 0.7 nm could be detected with a fraction of up to 88% of photons emitted into the ZPL. In addition, the observed colour centres feature count rates up to 4.8 Mcps, thus being the brightest diamond-based single photon sources to date. By performing spectroscopy at cryogenic temperatures, we verify the identification of these colour centres as SiV centres, measuring for the first time the fine structure splitting of a single SiV centre.

Acknowledgments

SEM analysis of the samples was performed by J Schmauch (Universität des Saarlandes, Saarbrücken, Germany) and M Fischer (Universität Augsburg, Germany). We thank L Marquant for help with the spin-coating procedure and R Albrecht (Universität des Saarlandes, Saarbrücken, Germany) for valuable help. The SiV structure in figure 1(a) was drawn by C Hepp (Universität des Saarlandes, Saarbrücken, Germany); B Weigand (Universität des Saarlandes, Saarbrücken, Germany) assisted with the g^2 fitting procedure. This work was financially supported by the Deutsche Forschungsgemeinschaft and the Bundesministerium für Bildung und Forschung (the network EphQuaM, contract no. 01BL0903).

References

[1] Gisin N, Ribordy G, Tittel W and Zbinden H 2002 *Rev. Mod. Phys.* **74** 145
[2] Kurtsiefer C, Mayer S, Zarda P and Weinfurter H 2000 *Phys. Rev. Lett.* **85** 290
[3] Rabeau J, Stacey A, Rabeau A, Prawer S, Jelezko F, Mirza I and Wrachtrup J 2007 *Nano Lett.* **7** 3433
[4] Beveratos A, Brouri R, Gacoin T, Poizat J and Grangier P 2001 *Phys. Rev.* A **64** 61802
[5] Wu E, Rabeau J R, Roger G, Treussart F, Zeng H, Grangier P, Prawer S and Roch J F 2007 *New J. Phys.* **9** 434
[6] Gaebel T, Popa I, Gruber A, Domham M, Jelezko F and Wachtrup J 2004 *New J. Phys.* **6** 98
[7] Wu E, Jacques V, Zeng H, Grangier P, Treussart F and Roch J R 2006 *Opt. Express* **14** 1296
[8] Rabeau J, Chin Y, Prawer S, Jelezko F, Gaebel T and Wrachtrup J 2005 *Appl. Phys. Lett.* **86** 131926
[9] Steinmetz D, Neu E, Hepp C, Albrecht R, Bolse W, Meijer J, Rogalla D and Becher C 2010 *Proc. SPIE* **7727** 77270P
[10] Aharonovich I, Zhou C, Stacey A, Orwa J, Castelletto S, Simpson D, Greentree A, Treussart F, Roch J F and Prawer S 2009 *Phys. Rev.* B **79** 235316
[11] Aharonovich I, Castelletto S, Simpson D A, Greentree A D and Prawer S 2010 *Phys. Rev.* A **81** 043813
[12] Aharonovich I, Castelletto S, Johnson B C, McCallum J C, Simpson D A, Greentree A D and Prawer S 2010 *Phys. Rev.* B **81** 121201
[13] Wang C, Kurtsiefer C, Weinfurter H and Burchard B 2006 *J. Phys. B: At. Mol. Opt.* **39** 37
[14] Jelezko F, Gaebel T, Popa I, Gruber A and Wrachtrup J 2004 *Phys. Rev. Lett.* **93** 130501
[15] Neumann P *et al* 2010 *Nat. Phys.* **6** 249
[16] Iakoubovskii K and Adriaenssens G 2000 *Diam. Relat. Mater.* **9** 1349
[17] Clark C D, Kanda H, Kiflawi I and Sittas G 1995 *Phys. Rev.* B **51** 16681
[18] Zaitsev A 2001 *Optical Properties of Diamond: A Data Handbook* (Berlin: Springer)
[19] Turukhin A V, Liu C H, Gorokhovsky A A, Alfano R R and Phillips W 1996 *Phys. Rev.* B **54** 16448
[20] Feng T and Schwartz B 1993 *J. Appl. Phys.* **73** 1415
[21] Goss J P, Jones R, Breuer S J, Briddon P R and Öberg S 1996 *Phys. Rev. Lett.* **77** 3041
[22] Sternschulte H, Thonke K, Sauer R, Münzinger P C and Michler P 1994 *Phys. Rev.* B **50** 14554
[23] Babinec T *et al* 2010 *Nat. Nanotechnol.* **5** 195
[24] Buchler B, Kalkbrenner T, Hettich C and Sandoghdar V 2005 *Phys. Rev. Lett.* **95** 063003
[25] Lukosz W and Kunz R 1977 *J. Opt. Soc. Am.* **67** 1607
[26] Vion C, Spinicelli P, Coolen L, Schwob C, Frigerio J M, Hermier J P and Maitre A 2010 *Opt. Express* **18** 7440
[27] Gsell S, Bauer T, Goldfuß J, Schreck M and Stritzker B 2004 *Appl. Phys. Lett.* **84** 4541
[28] Ruan J, Choyke W and Kobashi K 1993 *Appl. Phys. Lett.* **62** 1379
[29] Stacey A, Aharonovich I, Prawer S and Butler J 2009 *Diam. Relat. Mater.* **18** 51
[30] Bergman L, Stoner B, Turner K, Glass J and Nemanich R 1993 *J. Appl. Phys.* **73** 3951

[31] Fischer M, Brescia R, Gsell S, Schreck M, Brugger T, Greber T, Osterwalder J and Stritzker B 2008 *J. Appl. Phys.* **104** 123531
[32] Gorokhovsky A, Turukhin A, Alfano R and Phillips W 1995 *Appl. Phys. Lett.* **66** 43
[33] Wang C 2007 A solid-state single photon source based on color centers in diamond *PhD Thesis* Technische Universität, München
[34] Davies G 1981 *Rep. Prog. Phys.* **44** 787
[35] Walker J 1979 *Rep. Prog. Phys.* **42** 1605
[36] Sittas G, Kiflawi I, Kanda H and Spear P 1996 *Diam. Relat. Mater.* **5** 866
[37] Plakhotnik T, Moerner W, Palm V and Wild U 1995 *Opt. Commun.* **114** 83
[38] Fu K M C, Santori C, Barclay P E and Beausoleil R G 2010 *Appl. Phys. Lett.* **96** 121907
[39] Ha T, Laurence T, Chemla D and Weiss S 1999 *J. Phys. Chem.* B **103** 6839
[40] Alegre T P M, Santori C, Medeiros-Ribeiro G and Beausoleil R G 2007 *Phys. Rev.* B **76** 165205
[41] Fourkas J 2001 *Opt. Lett.* **26** 211
[42] Kitson S, Jonsson P, Rarity J and Tapster P 1998 *Phys. Rev.* A **58** 620
[43] Weaver J H, Olson C G and Lynch D W 1977 *Phys. Rev.* B **15** 4115
[44] Fleury L, Segura J, Zumofen G, Hecht B and Wild U 2000 *Phys. Rev. Lett.* **84** 1148